Bio-Design and Manufacturing (2021) 4:851–866
https://doi.org/10.1007/s42242-021-00159-y

RESEARCH ARTICLE

A novel wavy non-uniform ligament chiral stent with J-shaped stress–strain behavior to mimic the native trachea

Jiapeng Liu[1,2] · Xinhua Yao[1,2] · Zhenwei Wang[1,2] · Jian Ye[3] · Congcong Luan[1,2] · Jianzhong Fu[1,2] · Yong He[1,2]

Received: 29 March 2021 / Accepted: 11 July 2021 / Published online: 26 August 2021

Abstract

Tracheal stents are an important form of treatment for benign or malignant central airway obstruction. However, the mechanical behavior of current tracheal stents is significantly different from that of the native trachea, which leads to a variety of serious complications. In this study, inspired by the structure of the native trachea, a wavy non-uniform ligament chiral tracheal stent is proposed, in which J-shaped stress–strain behavior and negative Poisson's ratio response are achieved by replacing the tangential ligament of tetrachiral and anti-tetrachiral hybrid structure with a wavy non-uniform ligament. Through the combination of theoretical analysis, finite element analysis and experimental tests, a wide range of desired J-shaped stress–strain curves are explored to mimic the native porcine trachea by tailoring the stent geometry. Besides, the negative Poisson's ratio and auxetic diameter curves versus axial strain of the stent are also studied in detail, thus contributing to the enhancement of cross-section ventilation and reducing the migration of the stent. This novel tracheal stent with a unique microstructure shows a potential to perfectly match the physiological activities of the native trachea and thereby reduce potential complications.

Graphic abstract

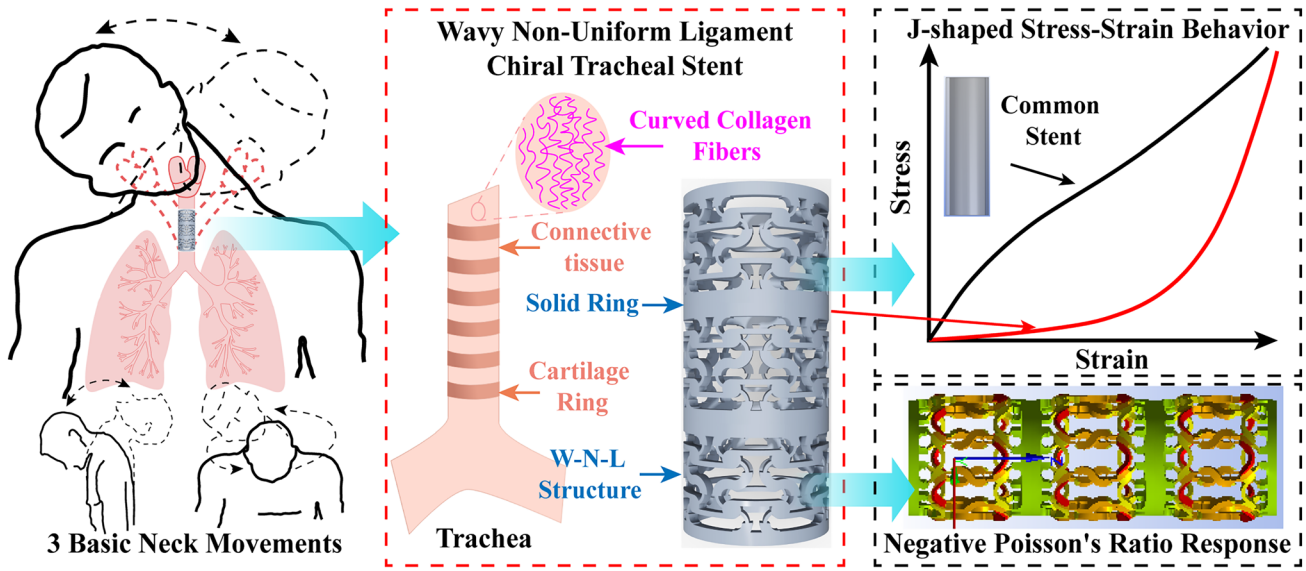

Keywords Tracheobronchial stenosis · Tracheal stent · Chiral auxetic structure · Wavy non-uniform ligament · J-shaped stress–strain behavior · Negative Poisson's ratio

Extended author information available on the last page of the article

Introduction

Tracheobronchial stenosis is one of the common critical diseases in the emergency department of respiratory critical care medicine and is mainly caused by focal or systemic inflammation, tuberculosis, dynamic collapse, or malignancy. Tracheal stents have been widely used in clinical treatment, because they can provide rapid and sustained relief of symptoms for most patients treated for malignant or benign tracheobronchial stenosis [1, 2]. Nowadays, in the clinical setting, tracheal stents mainly include metal stents and silicone stents. Among them, the former have been subject to warning by the US Food and Drug Administration (FDA), as it may pose a high risk of granulation tissue reaction, fracture, ischemic mucosal necrosis and perforation. Therefore, of the two types, more attention has been paid to the more widely applied silicone stents [3].

Unfortunately, the various complications (including migration, secondary stenosis, mucus plugging, inflammatory response and implant infection) after stent implantation have brought a huge burden to patients and the entire medical system [4]. Many of such complications are directly related to the mismatch of mechanical properties between the stent and the native trachea. The healthy tracheal length may extend by 20% in adults and by up to 46% in neonates during normal respiration or neck movements (Fig. 1a) [5, 6]. Moreover, the stress–strain curve of the trachea shows a typical J-shaped response when it is stretched (Fig. 1b) [7, 8]. Given these characteristics, there is a huge difference in the mechanical properties of existing common silicone stents and those of the native trachea. As shown in Fig. 1b, especially in the small strain region, the stress–strain curve of the common silicone stent is convex, which leads to its much larger stiffness than that of the native trachea. This results in inflammatory responses, migration, and strong foreign body sensation to the patient, reducing the quality of life [9–11]. Therefore, it is imperative to design a silicone stent with J-shaped stress–strain behavior to better mimic the mechanical properties of native trachea.

Owing to the interplay of elastin and collagen, the J-shaped stress–strain behavior widely exists in various biological tissues (e.g., skin [12], ligaments [13], blood vessels [14], tracheal tissue [7, 15, 16], etc.) that have curved and chained microstructures [8, 17]. Upon uniaxial stretching, this kind of stress–strain curve can be typically divided into three different regions (Fig. 1b) [12]. In the toe region, the curved and chained fibers begin to unfurl by bending and twisting, which leads to very little stiffness. As the strain increases, curved fibers gradually straighten in the heel region. Once the microstructures are fully extended in the linear region, the stress–strain curve will show a relatively linear response and a high tangent modulus [18]. In recent years, several bio-inspired soft-network microstructures (wavy or horseshoe ligament structure [19, 20], helical structures [17], or knitted structures [21]) were designed with the unique ability to precisely reproduce the J-shaped stress–strain behavior that is similar to native biological tissue. Among the designs, the wavy ligament structure has been widely studied in the field of flexible wearable electronics due to its retractable, programmable, and reconfigurable mechanical properties [22, 23]. The cylindrical stent has a unique J-shaped stress–strain behavior and, therefore, has shown potential as a medical implant stent [24, 25]. However, the single wavy ligament structure is considerably different from the structure of the trachea itself, and will cause a variety of complications, such as insufficient radial support, secondary stenosis, and difficulty in removal. Thus, a new tracheal stent structure is in need to match the J-shaped stress–strain behavior of the native trachea.

Chiral auxetic mechanical metamaterials have been studied extensively due to their unusual properties such as energy absorption, smart functionality, and negative Poisson's ratio (NPR). The chiral structure consists of nodes and tangentially connected ligaments. According to the number of ligaments and the way they are connected, this structure has many classifications, including trichirals, anti-trichirals, tetrachirals, anti-tetrachirals, and hexachirals [26, 27]. Recently, several modified chiral structures have been designed to meet the requirements of a wider range of applications. By changing the geometry of the node or the tangential ligament, the mechanical or thermal properties of the chiral structure can be enhanced, such that it can be applied in the fields of aerospace, microelectronics, or medical stents [28–30]. A tracheal stent with the NPR response will help ensure airway patency and enhance anti-migration performance. Thus, it is of great significance to design a tracheal stent with both J-shaped stress–strain behavior and NPR response.

In this study, a novel tracheal stent exhibiting the J-shaped stress–strain behavior and NPR response is designed with the aim to reduce the complications of common tracheal stents. Inspired by the structure of the native trachea, a wavy non-uniform ligament (W-N-L) chiral tracheal stent is proposed that mimics the mechanical properties of connective tissue by modifying its chiral structure with the wavy non-uniform ligament, as shown in Fig. 1c. A nonlinear mechanics model is developed to capture the effects of the key design parameters on the nonlinear mechanical responses of the W-N-L. Detailed finite element analysis (FEA) and experimental verification are carried out for the 2D and cylindrical stent structures to obtain the most optimal design parameters. The simultaneous presence of

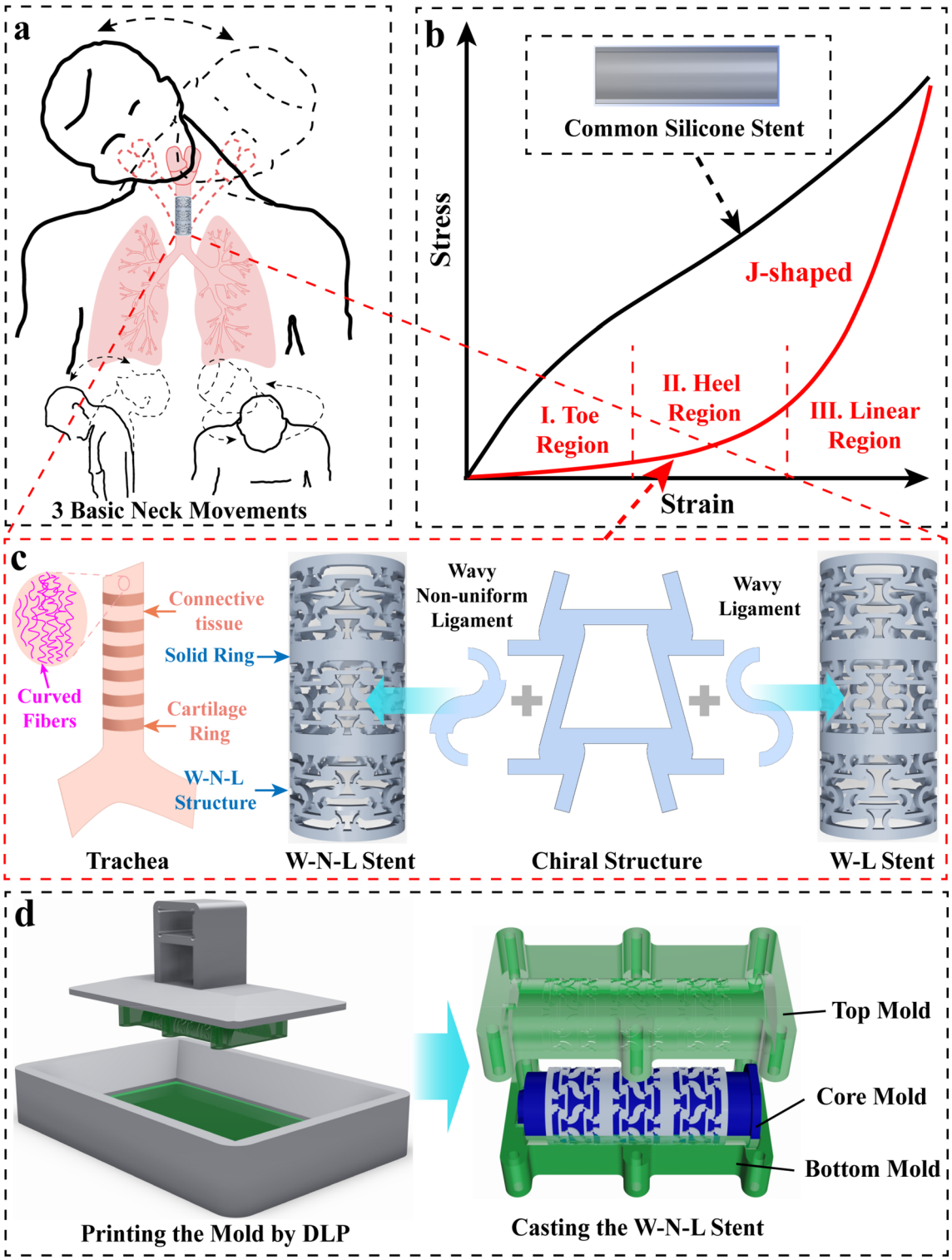

Fig. 1 Schematic diagram of the application and design of W-N-L chiral tracheal stent. **a** Schematic of tracheal deformation during neck movement. **b** Schematic of J-shaped stress–strain curve and stress–strain curve of common silicone tracheal stent. **c** Structure of wavy ligament chiral tracheal stent and wavy non-uniform ligament chiral tracheal stent inspired by the native trachea. **d** Preparation of the W-N-L stent using an indirect 3D printing process

J-shaped stress–strain behavior and NPR response reveals the superiority of the designed stent when compared with the existing stent, providing a feasible direction for next-generation tracheal stent designs.

Materials and methods

Design, analysis and fabrication of the proposed stent

The W-N-L chiral tracheal stent was designed using the commercial CAD software Creo 4.0 (Parametric Technology Corporation, USA). FEA was performed with the commercial software ANSYS Mechanical Workbench 18.0 (ANSYS, Inc., USA) to analyze the mechanical properties and deformation behavior of the ligament, two-dimensional (2D) structure, and stent. A hyperelastic constitutive model (Mooney–Rivlin model) was adopted to describe the employed high-modulus silicone materials. The values of the Mooney–Rivlin model parameters (C_{10} = 74,659 Pa, C_{01} = 3.90E + 05 Pa, C_{11} = 1.11E + 05 Pa, D_1 = 0 Pa^{-1}) were determined by fitting the measured uniaxial stress–strain curve following the international standard ISO 37: 2005.

The designed stent was prepared by an indirect 3D printing process that has been illustrated in detail in our previous study. In short, as shown in Fig. 1d, the negative structure molds were printed using a desktop 3D printer (BEBE2, NOVA3D, China) based on micro-digital light processing (DLP) technology using the standard rigid photosensitive resin purchased from the same company. The main printing parameters were set as layer thickness (0.05 mm), exposure time (10 s), *Z*-axis rising height (6.0 mm) and speed (100 mm/min), number of layers (4) and exposure time (60 s) of the bottom plate. The high-modulus liquid silicone rubber (LSR, E650, Hong Ye Jie Technology Co., Ltd (Shenzhen, China)) was then injected into the cavity of the mold and cured at 50 °C for more than 8 h. Subsequently, the silicone stent was re-cured at 80 °C for more than 4 h after its removal from the mold. The biocompatibility of the silicone material used for the stent has been verified in our previous article [31].

Evaluation of mechanical properties

The force–displacement curves were measured using a commercial mechanical testing machine (SUNS UTM-2203, Shenzhen, China), from which the stress–strain curves were calculated. A loading rate of 10 mm/min was set to ensure the nearly quasi-static deformation. Especially, the stent was fixed on the machine by a self-made fixture to reduce its deformation during clamping. A digital camera was used to record the deformation of the 2D structures and complete stents during the tensile test, and the transverse deformation under different tensile displacements was calculated using an image processing program (Image J). The Poisson's ratio could be calculated based on previous studies [32]. In brief, the longitudinal strain (ε_l) can be written as $\varepsilon_l = \left(L_{final} - L_{initial}\right)/L_{initial} \times 100\%$, and the transverse strain (ε_t) can be expressed as $\varepsilon_t = \left(D_{final} - D_{initial}\right)/D_{initial} \times 100\%$; the Poisson's ratio ($\nu_s$) of 2D structures and stents can be calculated by the equation $\nu_s = -\varepsilon_t/\varepsilon_l$. Here, the subscript 'initial' denotes the initial length, and the subscript 'final' denotes the length after deformation.

A porcine trachea was obtained from the local slaughterhouse to measure the anti-migration force of the stent by following the experimental method used in our previous paper. Specifically, two symmetrical holes were made at the top of the stent and fixed with metal wire for installation on the tensile testing machine. One end of the trachea was fixed on the bottom of the tensile machine, and the other end was kept unrestrained. The samples were then deployed in the porcine trachea with forceps, and the anti-migration force was recorded while the stent was pulled up from the porcine trachea.

Statistical analysis

All data were presented as the means ± standard deviation (SD). All experiments were carried out in at least quadruplicate, and the results were averaged. The statistical analysis was performed using one-way analysis of variance (ANOVA) followed by Tukey's post hoc test. $p < 0.05$ was considered as indicative of statistical significance.

Results

Design and mechanical analysis

This section aims to present the design and mechanical analysis of the W-N-L, the 2D W-N-L chiral structure, and the W-N-L chiral stent. Inspired by the curved and chained collagen fibers of native tracheal tissue, we developed a W-N-L chiral stent by combining the wavy ligament structure with the chiral structure. To mimic curved collagen fibers, the wavy uniform or non-uniform ligament was introduced to replace the stretched ligament of a tetrachiral and anti-tetrachiral hybrid structure, as shown in Fig. 1c. Then, as shown in Fig. 2, using this structural unit, a 2D W-N-L chiral structure was formed, and the ring unit and W-N-L chiral stent were further obtained. Figure 2a presents the basic geometric parameters of the W-N-L chiral stent. Its length and diameter can be designed individually according to the specific needs of patients. In order to match the native porcine trachea used in subsequent experimental verification, the outer diameter (D_{out}), inner diameter (D_{in}), and length

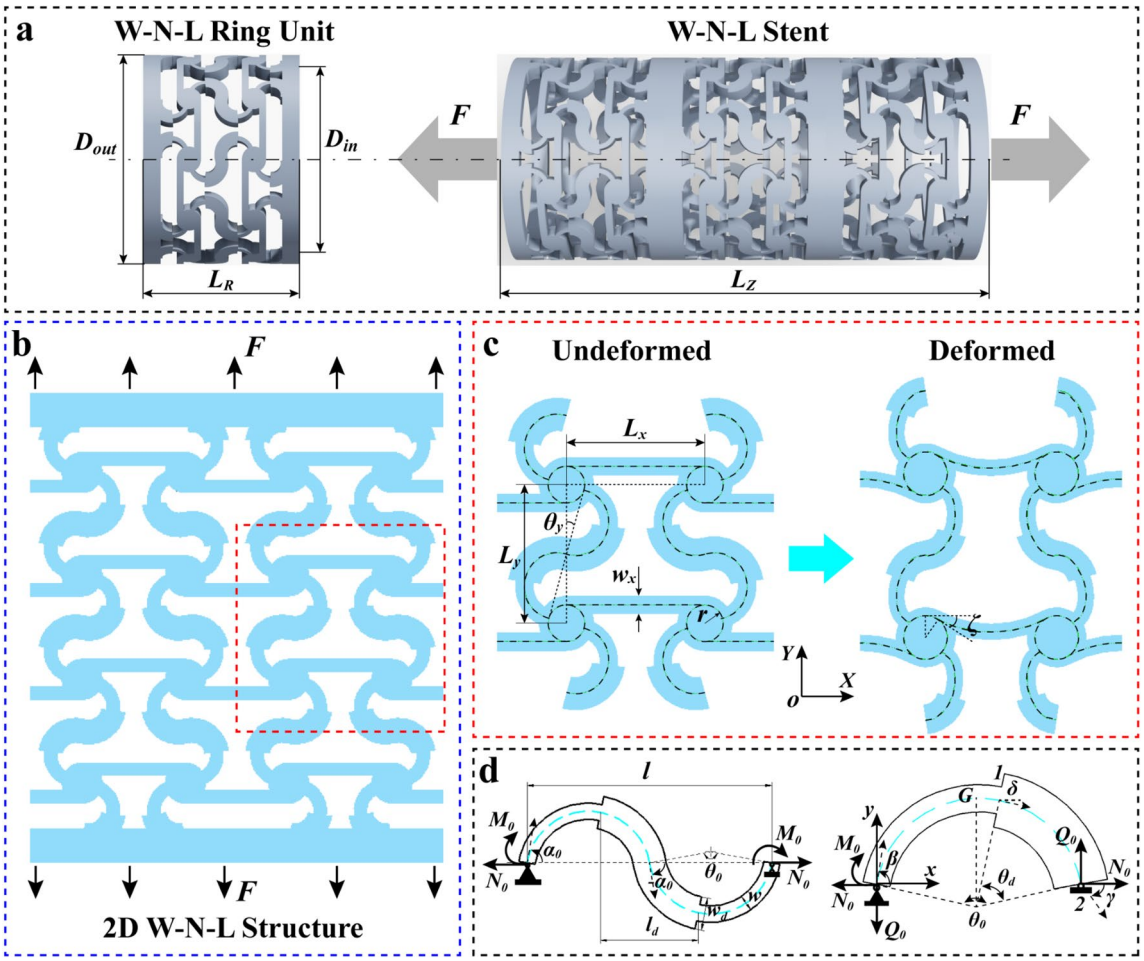

Fig. 2 Schematic of the design and mechanical model of the W-N-L chiral stent. **a** Geometric design parameters of the W-N-L chiral stent. **b** Structure and load diagram of 2D W-N-L chiral structure. **c** Undeformed and deformed diagram of the W-N-L chiral structure unit. **d** A simply supported W-N-L structure (and the left half) is subject to axial tension and a pair of antisymmetric moments

(L_Z) of the W-N-L stent were designed to be 24.0, 21.0, and 54.0 mm, respectively. Correspondingly, the length of the W-N-L ring unit (L_R) was 18.0 mm. The parameters of the tetrachiral and anti-tetrachiral hybrid structure could be determined based on the geometric parameters of the stent. As shown in Fig. 2c, the radius of the nodes (r) and the distance between nodes in the X (L_x) and Y (L_y) directions were 1.0, 7.1, and 7.5 mm, respectively. The thickness in the Z-direction (t) and ligament width in the X-direction (w_x) was 1.5 and 0.8 mm, respectively. The angle between the wavy ligament and the Y-direction (θ_y) could be easily obtained from the geometrical relation $\sin\theta_y = 2r/L_y$. The geometric parameters of the designed W-N-L chiral stent are listed in Table 1.

A finite-deformation model is introduced below for the W-N-L structure, with the focus on the effect of four independent parameters: arc angle (θ_0), width of the original ligament (w), length and width ratio ($\alpha_l = l_d/l$, $\tau = w_d/w$) of the widened section on the effective stress–strain behavior. As shown in Fig. 2c, the building block structure of the 2D W-N-L chiral structure deforms under stretching (Fig. 2b) with the nodes rotating, the X-direction ligaments bending, and the wavy ligaments gradually straightening. Here, the nodes can be assumed as rigid disks that rotate around their centers and do not undergo any deformations [33]. The W-N-L can be modeled as an Euler–Bernoulli beam due to its normalized width being usually smaller than 0.1. According to the deformation characteristics observed from FEA and experiments,

Table 1 Geometric parameters of the designed W-N-L chiral stent

D_{out} (mm)	D_{in} (mm)	L_Z (mm)	L_R (mm)	r (mm)	L_x (mm)	L_y (mm)	t (mm)	w_x (mm)	θ_0 (°)	w (mm)	$\alpha_l = l_d/l$	$\tau = w_d/w$
24.0	21.0	54.0	18.0	1.0	7.1	7.5	1.5	0.8	120–210	0.5–2.0	0.2–0.8	1.0–4.0

a simply supported ligament is subject to a force (N_0) along the axial direction and a pair of the antisymmetric moments (M_0) located at the two ends. Only half of the W-N-L is considered, as the geometry is antisymmetric with regard to the central point (Fig. 2d). For an infinitely small segment of the ligament, the length dS and tangential angle α in the undeformed state become ds and θ after deformation, respectively. The angles of α and θ are in the range of $[-\alpha_0, \alpha_0]$ and $[\beta, \gamma]$, respectively, where positive (negative) values denote a counterclockwise (clockwise) rotation from the X-axis. Subsequently, the effective strain and rotation angle can be expressed as $\varepsilon = (\mathrm{d}s - \mathrm{d}S)/\mathrm{d}S$, $\varphi = \theta - \alpha$, where $\mathrm{d}S = R_0\mathrm{d}\alpha$ and $\mathrm{d}s = r(\theta)\mathrm{d}\theta$. The R_0 and $r(\theta)$ represent the radius of the arc at the undeformed and deformed configurations, respectively.

According to previous research [19], the axial force N, shear force Q, and bending moment M in the beam at any cross section (Fig. 2d) can be calculated as:

$$N = E_sA\varepsilon = N_0\cos\theta + Q_0\sin\theta, \tag{1a}$$

$$Q = N_0\sin\theta - Q_0\cos\theta, \tag{1b}$$

$$M = E_sI\frac{\mathrm{d}\varphi}{\mathrm{d}S} = E_sI(1+\varepsilon)\frac{\mathrm{d}\varphi}{\mathrm{d}s}, \tag{1c}$$

The equilibrium equations of axial force, shear force, and bending moment in the beam satisfy [19, 20, 34]:

$$\frac{\mathrm{d}N}{\mathrm{d}s} + Q\frac{\mathrm{d}\theta}{\mathrm{d}s} = 0, \tag{3a}$$

$$\frac{\mathrm{d}Q}{\mathrm{d}s} - N\frac{\mathrm{d}\theta}{\mathrm{d}s} = 0, \tag{3b}$$

$$\frac{\mathrm{d}M}{\mathrm{d}s} - Q = 0. \tag{3c}$$

Substituting Eq. (1) into Eq. (3) and combining it with Eq. (2) gives:

$$\frac{\mathrm{d}^2\varphi}{\mathrm{d}S^2} = \left(1 + \frac{N_0\cos\theta + Q_0\sin\theta}{E_sA(S)}\right)\left(\frac{N_0}{E_sI(S)}\sin\theta - \frac{Q_0}{E_sI(S)}\cos\theta\right). \tag{4}$$

For the arc with an initial radius R_0, the initial curvature $K = \mathrm{d}\alpha/\mathrm{d}S$ is a constant, then $\frac{\mathrm{d}^2\varphi}{\mathrm{d}S^2} = \frac{\mathrm{d}^2\theta}{\mathrm{d}S^2}$. Thus, Eq. (4) becomes:

$$\frac{\mathrm{d}^2\theta}{\mathrm{d}S^2} = \left(1 + \frac{N_0\cos\theta + Q_0\sin\theta}{E_sA(S)}\right)\left(\frac{N_0}{E_sI(S)}\sin\theta - \frac{Q_0}{E_sI(S)}\cos\theta\right). \tag{5}$$

After integration on both sides, Eq. (5) becomes:

$$\left(\frac{\mathrm{d}\theta}{\mathrm{d}S}\right)^2 = \frac{-1}{E_s^2A(S)I(S)}\left[\left(N_0^2 - Q_0^2\right)\cos^2\theta + N_0Q_0\sin2\theta + 2E_sA(S)\left(N_0\cos\theta + Q_0\sin\theta\right)\right] + C, \tag{6}$$

where E_sA and E_sI are the tensile and bending stiffness, respectively. Here, for the stepped W-N-L, the cross-section area A and second moment I can be expressed as [34]:

$$A(S) = \begin{cases} tw & \left(0 < S < R_0\theta_0\left(1-\alpha_l\right)\right), \\ t(\tau w) & \left(R_0\theta_0\left(1-\alpha_l\right) < S < R_0\theta_0\right), \end{cases} \tag{2a}$$

where C represents a constant to be determined by boundary conditions. According to a previous study [35], at the left end of the ligament, $\left.\frac{\mathrm{d}\theta}{\mathrm{d}S}\right|_{S=0} = K_0 + \frac{M_0}{E_sI(S)}$, where K_0 is the initial curvature of the arc $K_0 = \frac{1}{R_0}$. Combined with Eq. (6), this gives:

$$\left(\frac{\mathrm{d}\theta}{\mathrm{d}S}\right)^2 = \left(K_0 + \frac{M_0}{E_sI(S)}\right)^2 + \frac{1}{2E_s^2A(S)I(S)}\left[\left(N_0^2 - Q_0^2\right)(\cos2\beta - \cos2\theta) + 2N_0Q_0(\sin2\beta - \sin2\theta)\right.$$
$$\left. + 4E_sA(S)N_0(\cos\beta - \cos\theta) + 4E_sA(S)Q_0(\sin\beta - \sin\theta)\right]. \tag{7}$$

$$I(S) = \begin{cases} \frac{tw^3}{12} & \left(0 < S < R_0\theta_0\left(1-\alpha_l\right)\right), \\ \frac{t(\tau w)^3}{12} & \left(R_0\theta_0\left(1-\alpha_l\right) < S < R_0\theta_0\right). \end{cases} \tag{2b}$$

In a similar fashion, at the right end of the ligament, $\left.\frac{\mathrm{d}\theta}{\mathrm{d}S}\right|_{S=R_0\theta_0} = K_2 + \frac{M_2}{E_sI(S)}$, where M_2 is the bending moment at the right end (two positions shown in Fig. 2d), which can be calculated as $M_2 = M|_{\theta=\gamma} = Q_0x_2 - N_0y_2$, and K_2 is the curvature of the arc at the right end, thus:

$$\left(\frac{\mathrm{d}\theta}{\mathrm{d}S}\right)^2 = \left(K_2 + \frac{M_2}{E_sI(S)}\right)^2 + \frac{1}{2E_s^2A(S)I(S)}\left[\left(N_0^2 - Q_0^2\right)(\cos2\gamma - \cos2\theta) + 2N_0Q_0(\sin2\gamma - \sin2\theta)\right.$$
$$\left. + 4E_sA(S)N_0(\cos\gamma - \cos\theta) + 4E_sA(S)Q_0(\sin\gamma - \sin\theta)\right], \tag{8}$$

where β and γ, respectively, represent the deformed angles at the left and right end. Simplifying the expression yields:

$$f(\beta,\theta)=\left(K_0+\frac{M_0}{E_sI(S)}\right)^2+\frac{1}{2E_s^2A(S)I(S)}\left[\left(N_0^2-Q_0^2\right)(\cos2\beta-\cos2\theta)+2N_0Q_0(\sin2\beta-\sin2\theta)\right.$$
$$\left.+4E_sA(S)N_0(\cos\beta-\cos\theta)+4E_sA(S)Q_0(\sin\beta-\sin\theta)\right], \tag{9}$$

$$g(\gamma,\theta)=\left(K_2+\frac{M_2}{E_sI(S)}\right)^2+\frac{1}{2E_s^2A(S)I(S)}\left[\left(N_0^2-Q_0^2\right)(\cos2\gamma-\cos2\theta)+2N_0Q_0(\sin2\gamma-\sin2\theta)\right.$$
$$\left.+4E_sA(S)N_0(\cos\gamma-\cos\theta)+4E_sA(S)Q_0(\sin\gamma-\sin\theta)\right]. \tag{10}$$

By the subsequent integration of Eq. (7) and Eq. (8) on both sides, we can obtain:

$$\int_\beta^\delta\frac{\mathrm{d}\theta}{\sqrt{f(\beta,\theta)}}=R_0\theta_0\left(1-\alpha_l\right), \tag{11}$$

$$\int_\delta^\gamma\frac{\mathrm{d}\theta}{\sqrt{g(\gamma,\theta)}}=R_0\theta_0\alpha_l, \tag{12}$$

where δ represents the deformed angle at the stepped position (one position shown in Fig. 1d). Then, the coordinates of the right end of the W-N-L after deformation can be calculated as:

$$\begin{Bmatrix}u_x\\u_y\end{Bmatrix}=\int_\beta^\delta\frac{1}{\sqrt{f(\theta,\beta)}}\cdot\left(1+\frac{N_0\cos\theta+Q_0\sin\theta}{E_sA(S)}\right)\cdot\begin{Bmatrix}\cos\theta\\\sin\theta\end{Bmatrix}\mathrm{d}\theta+\int_\delta^\gamma\frac{1}{\sqrt{g(\gamma,\theta)}}\cdot\left(1+\frac{N_0\cos\theta+Q_0\sin\theta}{E_sA(S)}\right)\cdot\begin{Bmatrix}\cos\theta\\\sin\theta\end{Bmatrix}\mathrm{d}\theta. \tag{13}$$

Moreover, at the top of the arc (i.e., point G in Fig. 2d), the deformed angle is 0. Thus, the following equation holds:

$$\int_\beta^0\frac{\mathrm{d}\theta}{\sqrt{f(\beta,\theta)}}=0.5R_0\theta_0\left(\alpha_l\le0.5\right)\text{ or }\int_0^\gamma\frac{\mathrm{d}\theta}{\sqrt{g(\gamma,\theta)}}=0.5R_0\theta_0\left(\alpha_l>0.5\right). \tag{14}$$

According to the load on the ligament, the simply supported boundary conditions are taken to investigate the stress–strain relation. In this case, the moment at the right end vanishes, i.e., $M_0=0$, $Q_0=0$. Then, the stress–strain relation can be obtained by defining the effective stress and strain of the ligament as $\sigma=N_0/A$ and $\varepsilon=u_x/\left(2R_0\sin\left(0.5\theta_0\right)\right)-1$. The above equations were solved using a user-developed MATLAB code.

J-shaped stress–strain behavior of W-N-L

As a result of the design flexibility enabled by the adjustment of microstructure geometries, the W-N-L can provide the desired stress–strain behaviors in a wide range. Figure 3 shows a collection of theoretical, FEA, and experimental results illustrating the effects of the above four dominant design parameters (arc angle (θ_0), ligament width (w), length ratio ($\alpha_l=l_d/l$), and width ratio ($\tau=w_d/w$) of the widened section). Both the results of FEA and experiment are in good agreement with the results predicted by the theoretical model, which verifies the accuracy of the theoretical model. It can be observed that the stress–strain curve of the ligament exhibits obvious nonlinear J-shaped behavior and has three deformation regions: toe region, heel region, and linear region (Fig. 1b). The stress is low at the toe region because the ligament essentially undergoes bending deformation. With the further increase in applied strain, the tangent direction of ligaments becomes gradually parallel to the load direction (Figs. 3e and 3f). At the same time, the deformation mode of the ligament gradually changes from bending deformation to stretching deformation, which leads to a rapid stress increase (heel region) and the ligament eventually exhibits a relatively linear stress–strain response (linear region).

The J-shaped stress–strain curve can be characterized by three key parameters. The critical strain, defined as $\varepsilon_{\mathrm{cr}}=\theta_0/[2\sin\left(0.5\theta_0\right)]-1$, marks the transition of deformation mode (dash-dot line). When the deformation of the ligament exceeds the critical strain, the ligament completely transforms into stretching deformation. The elastic moduli at the toe region (E_{toe}) and linear region (E_{linear}) are used to characterize the stiffness of the two regions separately. Based on the above equation, the critical strain only depends on the arc angle (θ_0) of the ligament. Figure 3a presents the J-shaped stress–strain curves of five different arc angles (θ_0) by fixing the width ($w=1.0\,\mathrm{mm}$) and without the widened section ($\tau=1.0$), as shown in Fig. 1b. With the increase in arc angle, the stress–strain curve shifts gradually downward and rightward. This shows the dependence of critical strain on arc angle, as

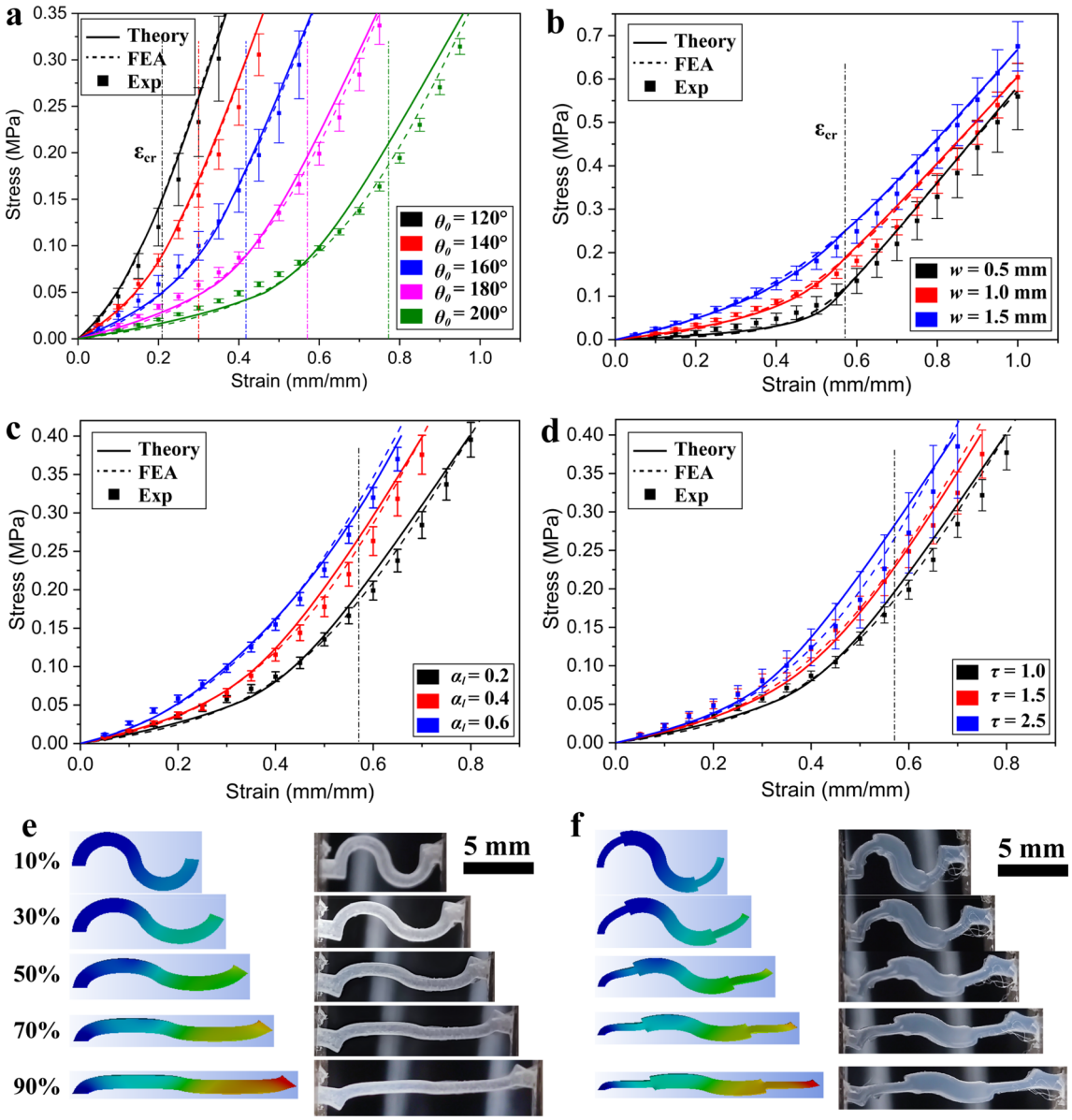

Fig. 3 Theoretical, FEA and experimental results of J-shaped stress–strain curves for W-N-L under uniaxial tension while changing the geometric parameters of **a** arc angle (θ_0); **b** ligament width (w); **c**, **d** length ratio (α_l), and width ratio (τ) of the widened section. **e**, **f** FEA and experimental images of the W-L **(e)** and W-N-L **(f)** under different uniaxial strains

ε_{cr} increases with the increase in θ_0. On the contrary, the effective stiffness of the ligament decreases as θ_0 increases. Both E_{toe} and E_{linear} gradually decrease with the increase in the θ_0, which is in agreement with previous research results [19]. In general, when θ_0 is fixed, in the bending deformation mode, the second moment of the cross section determines the effective stiffness, while in the stretching deformation mode, the section area dominates [25]. Thus, when the width of the ligament increases, the E_{toe} increases in turn, as shown in Fig. 3b. It is worth noting that, when the width of the ligament is small (e.g., 0.5 mm), the E_{linear} increases. This may be the result of the stiffening of the silicone rubber at higher stretches [36]. In addition, the elastic modulus of the material is varied to adapt to this phenomenon in the theoretical model [37]. As shown in Figs. 3c and 3d, as the values of α_l and τ increase, both E_{toe} and E_{linear} increase when θ_0 and w are fixed, which is consistent with a previous study [30]. Thus, the existence of the widened section in the wavy ligament provides a solution to enable a wider range of effective stiffness in the J-shaped stress–strain curve. Notably, when τ increases, the E_{linear} rises faster than E_{toe}, which is beneficial for simulating the mechanical properties of the native trachea.

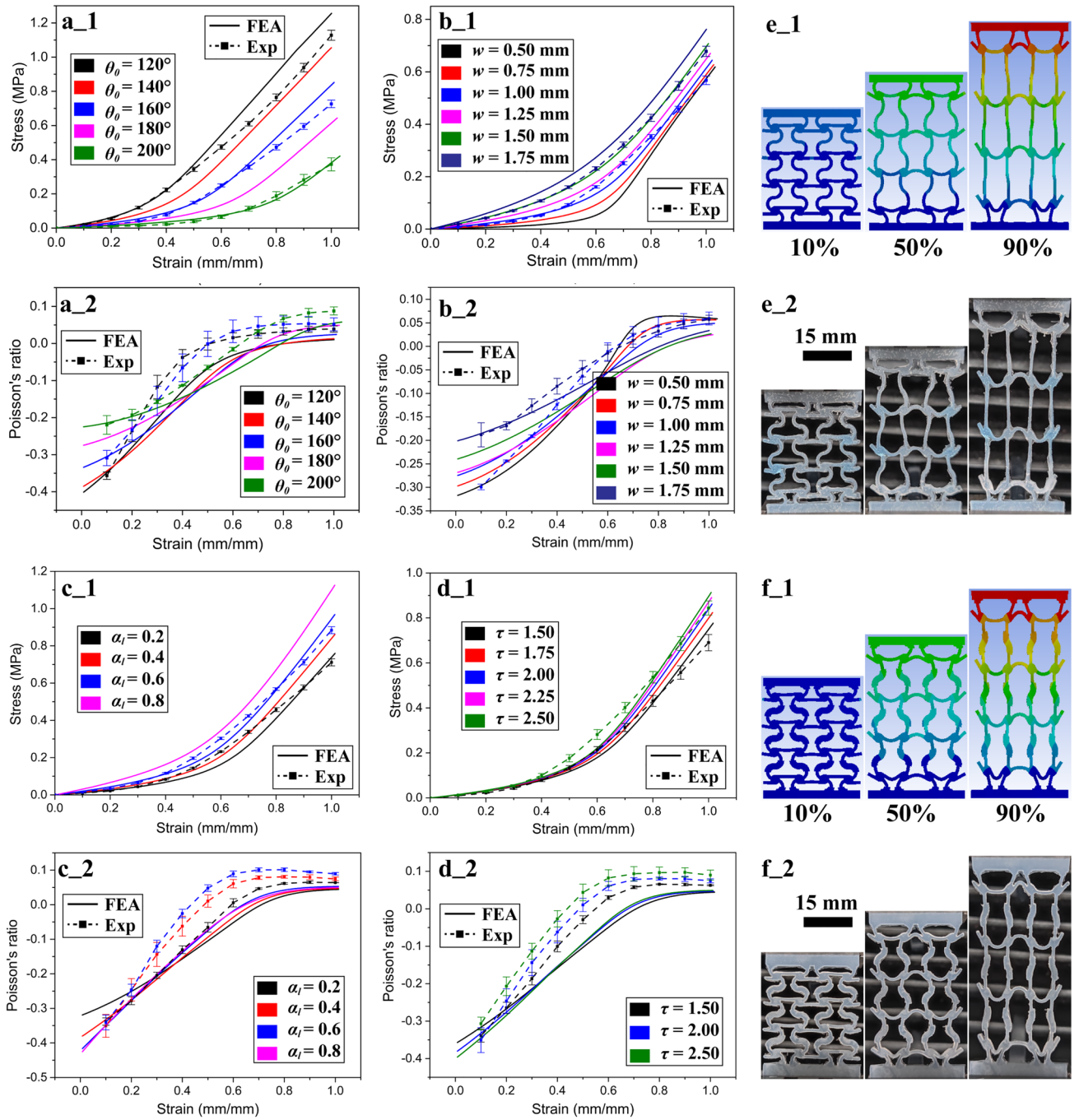

Fig. 4 The J-shaped stress–strain curves and the Poisson's ratio of the 2D W-N-L chiral structure. **a**, **b** The stress (a_1, b_1) and Poisson's ratio (a_2, b_2) of the 2D W-L structure versus applied strain for different arc angles (θ_0) and wavy ligament widths (w). **c**, **d** The stress (c_1, d_1) and Poisson's ratio (c_2, d_2) of the 2D W-N-L structure versus applied strain for different length ratios (α_l) and width ratios (τ) of the widened section. **e**, **f** FEA (e_1, f_1) and experimental (e_2, f_2) images of the 2D W-L chiral structure **(e)** and 2D W-N-L chiral structure **(f)** under different strain levels

Mechanical properties of 2D W-N-L structure

The stress–strain curves and Poisson's ratio of the 2D W-N-L chiral structure are presented in Fig. 4. After replacing the ligaments of the tetrachiral and anti-tetrachiral hybrid structure with the W-L or W-N-L, the deformation behavior of the 2D W-N-L chiral structure is changed compared with the original chiral structure. As shown in Figs. 4e and 4f, in addition to the bending of the transverse ligaments and the rotation of the nodes [29], the wavy ligaments in the

stretching direction undergo a transition from bending deformation to stretching deformation. The stress–strain curve and Poisson's ratio of the 2D W-L structure are discussed focusing on the arc angle (θ_0) and the width of the wavy ligament (w). The stress–strain behavior of the 2D W-L structure still shows the typical J-shaped response, which means that the bending of the transverse ligament has little effect on it. Besides, the influence of θ_0 and w on the stress–strain behavior is similar to that for W-N-L (Figs. 4a_1 and 4b_1). Figures 4a_2 and 4b_2 reveal the FEA and experimental results of the effect of θ_0 and w on the Poisson's ratio of the 2D W-L structure. The results of the experiment basically agree with those of FEA; however, within the intermediate strain range (about 0.3–0.6), the experimental value is greater than the FEA value. This may be caused by errors introduced by the sample preparation and measurement process. In general, the Poisson's ratio of the 2D W-L structure shows a similar trend with the increase in tensile strain. As the strain increases, the Poisson's ratio gradually changes from negative to positive. Notably, all of the Poisson's ratio curves gradually approach 0 ($-0.05 \sim +0.05$) in the end. This outstanding NPR or zero Poisson's ratio feature has attracted widespread attention in many fields, especially in biomedical implants [27, 38]. Specifically, in the low-strain area, as the θ_0 increases, the absolute Poisson's ratio of the 2D W-L structure decreases, whereas this trend is opposite for the large-strain area (Fig. 4a_2). This means that the smaller the θ_0, the more violent the Poisson's ratio change in the intermediate strain region. Meanwhile, the effect of w on Poisson's ratio is different. As its value increases, the Poisson's ratio curves become more gentle (Fig. 4b_2). When $\tau > 1.0$, the width of the wavy ligament is stepped, as shown in Fig. 4f. The effect of the length ratio (α_l) and width ratio (τ) of the widened section of the 2D W-N-L chiral structure on the J-shaped stress–strain curves is similar to that for the single ligament (Figs. 4c_1 and 4d_1). What is even more noteworthy is that these two parameters have little effect on the Poisson's ratio of the 2D structure; therefore, we can use them to adjust the stress–strain behavior of the structure under the premise of ensuring that its Poisson's ratio remains almost unchanged, which is of great significance for expanding the application scope of the 2D W-N-L structure.

W-N-L chiral tracheal stent

In this section, the J-shaped stress–strain behavior and NPR response of this new tracheal stent is described in detail. To establish the optimal geometric parameters of the W-N-L chiral tracheal stent, the effects of the above-mentioned four parameters on the stress–strain curves and Poisson's ratio are quantitatively assessed under stretching using FEA. First, the curves of the axial effective stress, radial diameter, and Poisson's ratio versus axial strain of the stent with different arc angle ($\theta_0 = 120°$, 150°, 180°, 210°) are presented in Fig. 5a. Predictably, as the θ_0 increases, the elastic moduli of the toe region (E_{toe}) and linear region (E_{linear}) decrease, and the critical strain (ε_{cr}) shifts to the right. As shown in Fig. 5a_2, the reduction rates of E_{toe} and E_{linear} with the increase in θ_0 are almost the same. Therefore, although θ_0 has the greatest effect on the J-shaped stress–strain curve, it is impossible to separately adjust a certain characteristic parameter. As shown in Fig. 5a_3, due to the inconsistency of the Poisson's ratio under different θ_0 values for the low-strain, medium-strain and high-strain regions, the radial diameter of the stent shows a similar trend. The smaller the θ_0, the faster the diameter reaches the maximum, and the final diameter will be also larger. This also means that the strain range where it can maintain positive changes is also narrower.

Second, Fig. 5b shows the curves of the axial effective stress, radial diameter, and Poisson's ratio versus the axial strain of the stent with different axial ligament widths ($w = 0.5$, 1.0, 1.5, 2.0 mm) with the fixed value of $\theta_0 = 180°$. Unlike θ_0, w has no effect on the critical strain, and the changing trends of E_{toe} and E_{linear} are also different. As shown in Fig. 5b_2, E_{toe} gradually increases with the increase in w, while the change of E_{linear} is smaller; when $w = 0.5$mm, there is a significant increase, which has also been reported in previous studies [33, 39]. This can be used to adjust the elastic modulus of the stent under the premise of fixed ε_{cr}. As shown in Fig. 5b_3, the Poisson's ratio and w are positively correlated; conversely, its diameter and Poisson's ratio are negatively correlated. When $w = 0.5$mm, the Poisson's ratio curve shows a different corner in the low strain stage, but it has little effect on the diameter.

Third, as shown in Figs. 5c and 5d, a variety of length ratios ($\alpha_l = 0.2$, 0.4, 0.6, 0.8) and width ratios ($\tau = 1.0$, 2.0, 3.0, 4.0) are taken into account separately, while the arc angle and width are fixed as $\theta_0 = 180°$, and $w = 0.5$ mm. Since these two parameters adjust the mechanical behavior of the stent by setting the width of the axial ligament, their effects on the stress–strain curve of the stent are similar. Compared with the uniform ligament, the increase in α_l and τ will significantly enhance the axial stiffness of the stent, especially in the linear region of the J-shaped stress–strain curves shown in Figs. 5c_2 and 5d_2. When the α_l and τ are increased, the curves of diameter and Poisson's ratio show similar trends with the increase in w. It should be noted that, when $\tau = w_d/w = 1.0$, the ligament is uniform; therefore, the curve of $\tau = 1.0$ in Fig. 5d is exactly the same as the curve of $w = 0.5$ mm in Fig. 5b. By comparison, it can be clearly seen that the increase in τ value has a smaller effect on Poisson's ratio and diameter than the direct increase in w. What is more, E_{linear} is increased by the stepped widened section, whereas E_{toe} is less affected, which is conducive to mimicking the J-shaped stress–strain behavior of native trachea using the W-N-L chiral stent. In our previous paper,

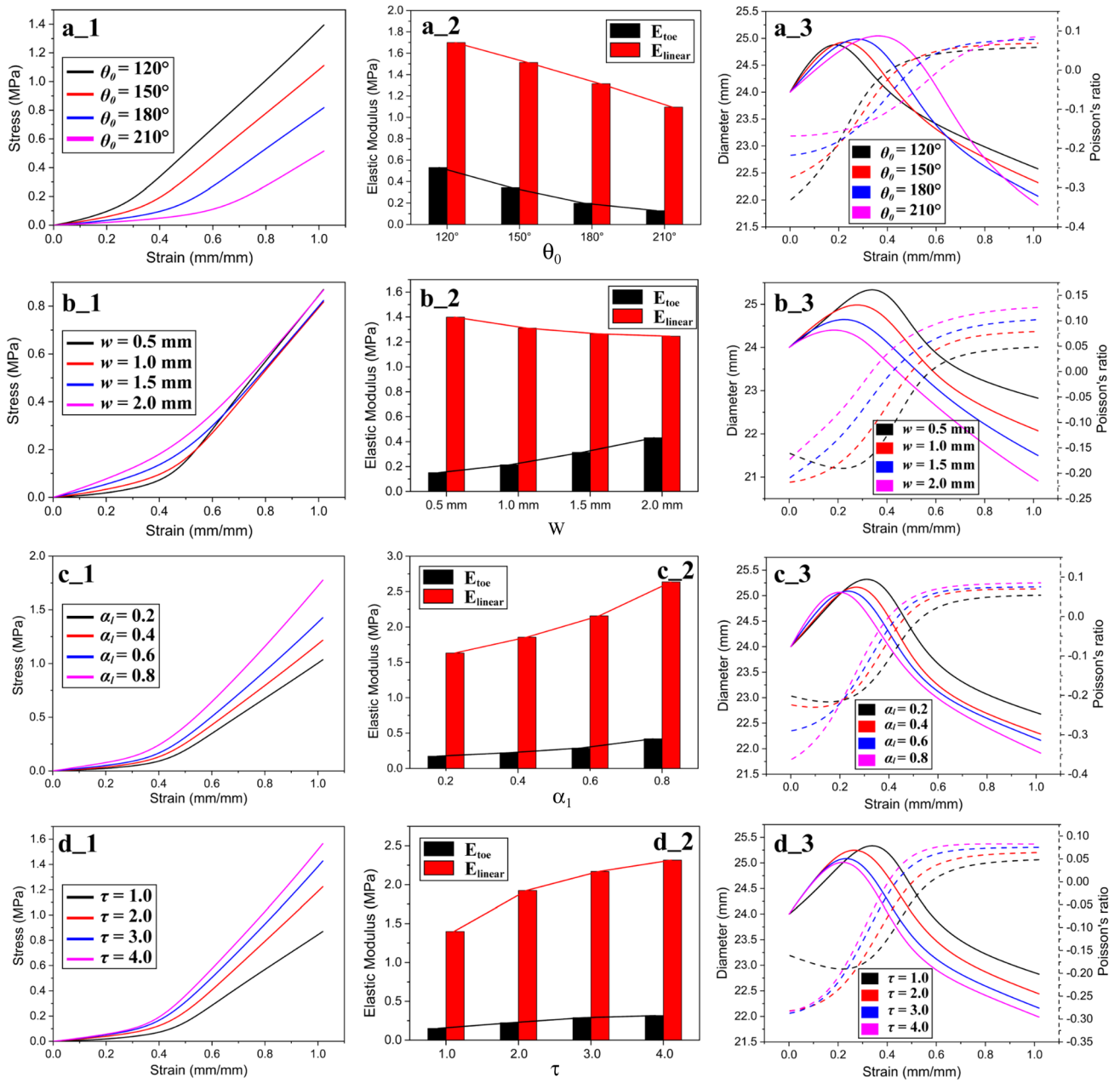

Fig. 5 FEA results of the J-shaped stress–strain, Poisson's ratio, and diameter curves of the W-N-L chiral tracheal stent under uniaxial stretching. **a** Stress–strain curves (a_1), elastic modulus histogram (a_2), and Poisson's ratio and diameter curves (a_3) for a wide range of arc angles (θ_0) with a fixed value of $w = 1.0$ mm. **b** Stress–strain curves (b_1), elastic modulus histogram (b_2), and Poisson's ratio and diameter curves (b_3) for different ligament widths (w) with a fixed value of $\theta_0 = 180°$. **c** Stress–strain curves (c_1), elastic modulus histogram (c_2), and Poisson's ratio and diameter curves (c_3) for different length ratios (α_l) of the widened section with fixed values of $\theta_0 = 180°$, $w = 0.5$ mm, and $\tau = 3.0$. **d** Stress–strain curves (d_1), elastic modulus histogram (d_2), and Poisson's ratio and diameter curves (d_3) for different width ratios (τ) of the widened section with fixed values of $\theta_0 = 180°$, $w = 0.5$ mm, and $\alpha_l = 0.6$

we analyzed the mechanical properties of a tetrachiral and anti-tetrachiral hybrid stent in detail [31]. The chiral stent has a similar auxetic effect, but its stress–strain curve is close to linear. This further proves that the introduction of the wave uniform or non-uniform ligament brings a J-shaped stress–strain behavior to the stent proposed in this paper.

When carefully comparing the W-N-L chiral tracheal stents and the 2D W-N-L structure, we can find that, when the 2D structures are bent into tubular structures, some of their mechanical properties will change. In order to be consistent with the structure of the native trachea, we employed the Y-axis as the rotation axis to bend the 2D structure.

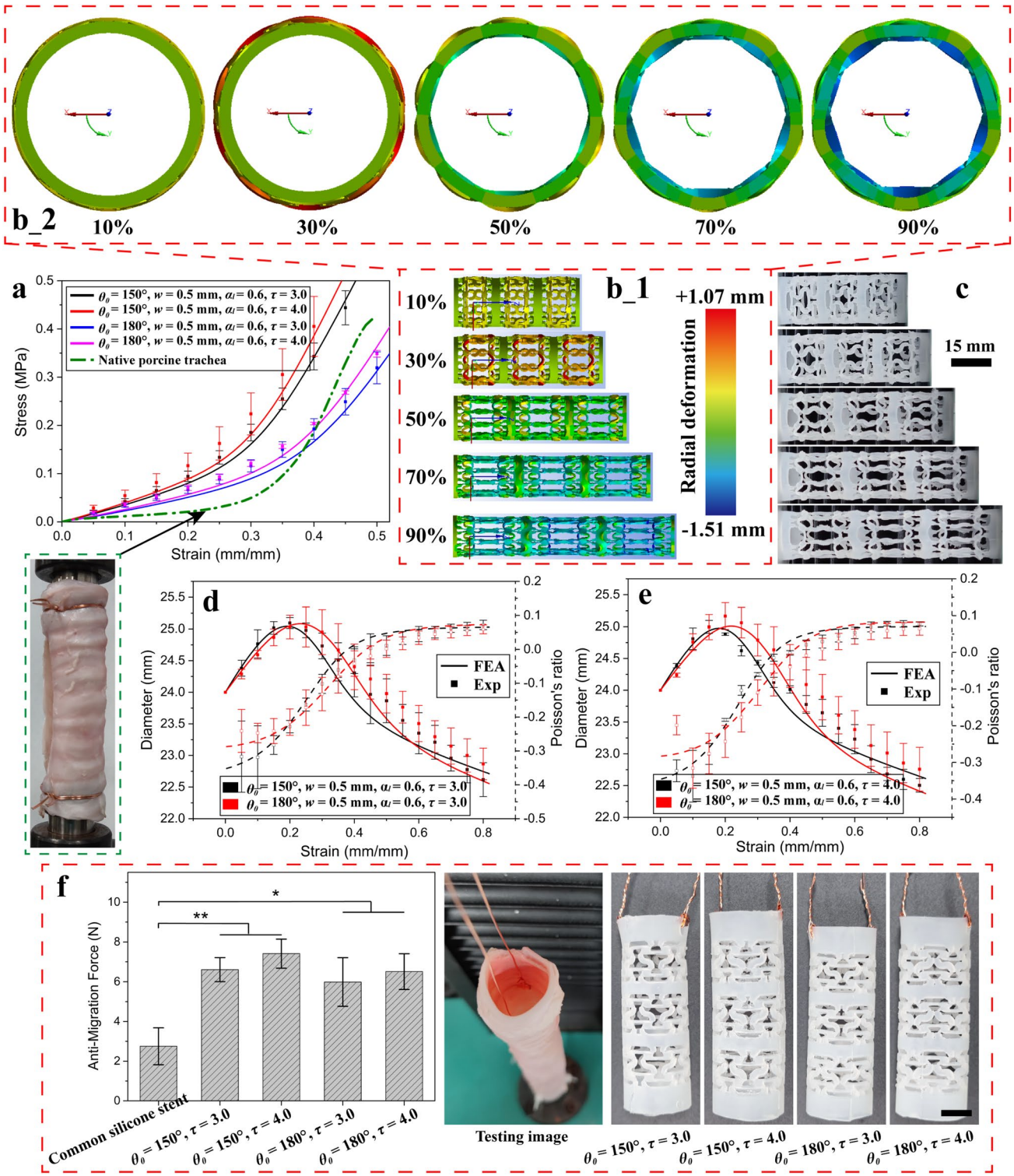

Fig. 6 Experimental and FEA results of the W-N-L chiral tracheal stent and native porcine trachea under axial stretching. **a** The J-shaped stress–strain curves of the stent and trachea (insert: image of axial stretched native porcine trachea). **b** FEA main view (b_1) and top view (b_2) images of the stent under different strain levels. **c** Experimental images of the stent under different strain levels. **d**, **e** The diameter and Poisson's ratio curves of the stent versus axial strain. **f** Anti-migration force of the stents in a porcine trachea (right: images of anti-migration testing and samples, scale bar: 10 mm), $*p<0.05$, $**p<0.01$

Therefore, the wave ligaments in the structure were always distributed along the direction of the force (*Y*-direction in the 2D structure and axial direction in the tubular structure). In this manner, no significant changes occurred in the stress–strain behavior of the 2D structure and the stent. On the other hand, the transverse ligaments changed from the horizontal distribution of the plane to the circumferential distribution of the cylinder, which caused a change in the Poisson's ratio. As shown in Figs. 4 and 5, with the change of θ_0, the difference in Poisson's ratio between the 2D and tubular structure is not obvious; however, with the change of w, α_l, and τ, the Poisson's ratio curves of the two structures deviate significantly. For the W-N-L chiral tracheal stents, the influence of w on Poisson's ratio is more regular, and the curves do not have multiple intersections. In addition, the influence of α_l, and τ on the Poisson's ratio curve is more obvious compared with that for 2D structures, which is more conducive to the ability to adjust the Poisson's ratio of the W-N-L chiral tracheal stents.

In order to guide the selection of the geometric parameters of the stent, a uniaxial tensile test was carried out on a native porcine trachea (Fig. 6a). It was selected due to its proven excellent preclinical features in terms of geometry, biomechanics and biochemistry [6, 40]. According to these test results and the above analysis of the geometric parameters of the W-N-L chiral stent, four groups of typical design parameters, namely, $\theta_0 = 150°$ and 180°, $\tau = 3.0$ and 4.0, $w = 0.5$ mm, and $\alpha_l = 0.6$ were selected. The designed stents were prepared by an indirect 3D printing method ($n = 4$), and their stress–strain behavior, diameter, and Poisson's ratio were further measured. As shown in Fig. 6a, the experimental results are in good agreement with the FEA results for the stress–strain curves under stretching. The stress–strain curve of the W-N-L chiral stent shows a J-shaped response, which is close to that of the native porcine trachea. Due to material and preparation process limitations, there is still a small gap between the stress–strain curve of the stent and the native trachea. The main differences are that the stent is harder in the toe region and softer in the linear region. However, this result is still a considerable improvement compared with the common tracheal stent.

As shown in Figs. 6d and 6e, the results for stent diameter and Poisson's ratio were also evaluated, and they agree well with the FEA results. The stent shows obvious NPR behavior in that its diameter is larger than the original diameter before reaching about 40% of the tensile strain, which is consistent with the top view of the deformed stent (Fig. 6b_2). In addition, Figs. 6b and 6c show the FEA and experimental images of the stent under different degrees of axial strain (more details can be found in Video S1). The deformation behavior of the stent in the experiment is completely consistent with the FEA result, and is similar to that of the 2D W-N-L chiral structure (Fig. 4f). As shown in Fig. 6f, we implanted the prepared W-N-L chiral tracheal stents ($\theta_0 = 150°, \tau = 3.0, \theta_0 = 150°, \tau = 4.0, \theta_0 = 180°, \tau = 3.0$, and $\theta_0 = 180°, \tau = 4.0$) into a porcine trachea in order to verify whether the auxetic effect could increase the anti-migration force to prevent slippage. Compared with the common silicone stent, the anti-migration ability of the designed stent is significantly increased, benefiting from the negative Poisson's ratio effect. In addition, when $\theta_0 = 150°$, the anti-migration force of the stent is slightly greater than $\theta_0 = 180°$ due to its greater stiffness, as shown in Fig. 6a.

Discussion

Herein, a W-L-N chiral tracheal stent was designed by replacing the tangential ligament of the chiral structure with the W-N-L. The results show that this confers the unique J-shaped stress–strain behavior and NPR response on the tracheal stent. A tracheal stent with a J-shaped stress–strain behavior that can match the mechanical properties of the native trachea is undoubtedly of great significance in reducing inflammation and improving the quality of life of patients. Meanwhile, its NPR response provides the potential to help better maintain an unobstructed airway while reducing the migration of the stent and even adapting to the tracheal growth of pediatric patients.

Inspired by the curved and chained microstructures of many biological tissues, several soft network structures with J-shaped stress–strain response have been proposed. However, most of these are used in 2D flexible electronics, and their application to the field of implants, such as tracheal stents, is still an unexplored direction [41]. Recently, a class of biomimetic three-dimensional (3D) periodically arranged helical microstructure network was proposed, which can reproduce the nonlinear stress–strain response of biological tissues [17]. Unfortunately, the value of this structure can only be utilized in the field of medical implants or tissue engineering when the 3D printing technology achieves a breakthrough of producing the helical structure with the same scale as the collagen fiber [42]. In the present work, inspired by the native tracheal structure (cartilage + connective tissue), we designed the tracheal stent by bending a 2D W-N-L chiral structure into a cylindrical shape. Since the stiffness of the cartilage ring is much greater than that of the connective tissue, the axial J-shaped stress–strain behavior of the trachea is mainly determined by the mechanical properties of the connective tissue [43, 44]. Thus, as shown in Fig. 2a, the solid ring on the stent was used to simulate the cartilage ring, and the W-N-L chiral structure between the rings determines the axial stress–strain behavior of the stent, just like in connective tissue. In follow-up research, a hard polymer ring can be embedded in the solid ring to provide a stronger radial support force, such as the cartilage ring

with the help of a finer direct 3D printing process [45, 46]. Furthermore, if biocompatible and degradable materials are used to prepare this structure, it will benefit from a nonlinear mechanical response closely matched with that of the native trachea, and thus bear the potential for serving as an ideal framework of the tissue-engineered trachea.

The optimal NPR response of auxetic mechanical metamaterials results in their outstanding mechanical characteristics (fracture and indentation resistance, energy absorption, and acoustic and vibration properties); therefore, they have been utilized in a wide range of applications (biomedical devices, flexible electronic sensors and actuators) [27, 47]. In this paper, the chiral structure is constructed from a variety of auxetic mechanical metamaterials (such as chiral, re-entrant, and rotating rigid structures) as the basis of the tracheal stent, because its node rotation and ligament bending deformation features can thus be easily combined with the wavy ligament [26]. By replacing the tangential ligament in the chiral hybrid structure with a wavy-shaped ligament (Fig. 1c), it is straightforward to integrate the two sets of outstanding mechanical features of J-shaped stress–strain behavior and NPR response. This combination allows the W-N-L chiral stent to better adapt to the deformation of the trachea during the physiological activities of the patient, to resist migration, and to ensure a larger ventilation section compared to previously proposed stents [29, 48, 49].

Our results have proved the unique advantages of the designed stent, while the following issues need further clarification before clinical application can be implemented. First, although our previous studies have proved the biocompatibility of the materials used herein [31], their unknown effects on tissues when implanted in vivo prompt further experimental studies. Second, the establishment of a theoretical mechanical model for the final stent will be more helpful for the analysis and optimization of the geometric parameters. Finally, whether this novel stent will cause unexpected complications will also need to be addressed. Although there are issues to resolve, the W-N-L chiral stent undoubtedly offers a feasible approach for reducing the complications of existing tracheal stents.

Conclusions

In summary, inspired by the structure of the native trachea, a W-N-L chiral tracheal stent was designed by combining W-N-L, tetrachiral and anti-tetrachiral hybrid structure, and prepared by an indirect 3D printing process. A comprehensive evaluation based on mechanical analysis, FEA, and experimental measurements clarified the effects of the geometric parameters of the wavy ligament and the lattice topology on the J-shaped stress–strain behavior of the stent. The comparison of the designed stent with the porcine trachea showed that it can well match the nonlinear mechanical response of the native trachea. Furthermore, the negative Poisson's ratio of the stent resulted in its diameter still being larger than the original diameter under more than 40% axial strain, which plays a crucial role in keeping the airway open and reducing stent migration. These findings prove that the proposed stent with J-shaped stress–strain behavior and negative Poisson's ratio response has a great potential for generating a novel tracheal stent for clinical application with the aim of curing tracheobronchial stenosis.

Supplementary Information The online version contains supplementary material available at https://doi.org/10.1007/s42242-021-00159-y.

Acknowledgements This article was supported by the National Key Research and Development Program of China (No. 2020YFC1107103), the National Natural Science Foundation of China (No. 51821093), and the Research Project of Public Welfare Technology Application of Zhejiang Province, China (No. LGF21H010006).

Author contributions JPL contributed to conceptualization, formal analysis, data curation, investigation, methodology, visualization and writing—original draft; XHY and JY contributed to conceptualization, supervision, validation, and writing—review & editing; ZWW and CCL helped in formal analysis and methodology; JZF and YH helped in resources, supervision, validation and project administration.

Declarations

Conflict of interest All authors declare that there is no financial or commercial conflict of interest.

Ethical approval This article does not contain any studies with human or animal subjects performed by any of the authors.

References

1. Murgu SD, Egressy K, Laxmanan B et al (2016) Central airway obstruction benign strictures, tracheobronchomalacia, and malignancy-related obstruction. Chest 150(2):426–441. https://doi.org/10.1016/j.chest.2016.02.001
2. Milian RD, Foley E, Bauer M et al (2019) Expiratory central airway collapse in adults: corrective treatment (part 2). J Cardiothorac Vasc Anesth 33(9):2555–2560. https://doi.org/10.1053/j.jvca.2018.09.009
3. Avasarala SK, Freitag L, Mehta AC (2019) Metallic endobronchial stents a contemporary resurrection. Chest 155(6):1246–1259. https://doi.org/10.1016/j.chest.2018.12.001
4. Guibert N, Saka H, Dutau H (2020) Airway stenting: technological advancements and its role in interventional pulmonology. Respirology 25(9):953–962. https://doi.org/10.1111/resp.13801
5. Kamel KS, Beckert LE, Stringer MD (2009) Novel insights into the elastic and muscular components of the human trachea. Clin Anat 22(6):689–697. https://doi.org/10.1002/ca.20841
6. Boazak EM, Auguste DT (2018) Trachea mechanics for tissue engineering design. Acs Biomater Sci Eng 4(4):1272–1284. https://doi.org/10.1021/acsbiomaterials.7b00738

7. Baiguera S, Del Gaudio C, Jaus MO et al (2012) Long-term changes to in vitro preserved bioengineered human trachea and their implications for decellularized tissues. Biomaterials 33(14):3662–3672. https://doi.org/10.1016/j.biomaterials.2012.01.064
8. Guimaraes CF, Gasperini L, Marques AP et al (2020) The stiffness of living tissues and its implications for tissue engineering. Nat Rev Mater 5(5):351–370. https://doi.org/10.1038/s41578-019-0169-1
9. Wong VW, Paterno J, Sorkin M et al (2011) Mechanical force prolongs acute inflammation via T-cell-dependent pathways during scar formation. FASEB J 25(12):4498–4510. https://doi.org/10.1096/fj.10-178087
10. Karush JM, Seder CW, Raman A et al (2017) Durability of silicone airway stents in the management of benign central airway obstruction. Lung 195(5):601–606. https://doi.org/10.1007/s00408-017-0023-4
11. Wu XD, Zhang X, Zhang W et al (2019) Long-term outcome of metallic stenting for central airway involvement in relapsing polychondritis. Ann Thorac Surg 108(3):897–904. https://doi.org/10.1016/j.athoracsur.2019.02.039
12. Yang W, Sherman VR, Gludovatz B et al (2015) On the tear resistance of skin. Nat Commun 6:10. https://doi.org/10.1038/ncomms7649
13. Kwansa AL, Empson YM, Ekwueme EC et al (2010) Novel matrix based anterior cruciate ligament (ACL) regeneration. Soft Matter 6(20):5016–5025. https://doi.org/10.1039/c0sm00182a
14. Chamiot-Clerc P, Copie X, Renaud JF et al (1998) Comparative reactivity and mechanical properties of human isolated internal mammary and radial arteries. Cardiovasc Res 37(3):811–819. https://doi.org/10.1016/s0008-6363(97)00267-8
15. Meyers AD, Bishop HE, Peters S (1980) Biomechanical characteristscs of the human trchea. Otolaryngology-Head Neck Surg 88(4):409–411. https://doi.org/10.1177/019459988008800416
16. Lomeli-Mejia PA, Cruz-Orea A, Araujo-Monsalvo VM et al (2020) Evaluation of tensile force in a porcine trachea using a reflective optical method. J Spectroscopy 2020:7816969. https://doi.org/10.1155/2020/7816969
17. Yan DJ, Chang JH, Zhang H et al (2020) Soft three-dimensional network materials with rational bio-mimetic designs. Nat Commun 11(1):11. https://doi.org/10.1038/s41467-020-14996-5
18. Ma YJ, Feng X, Rogers JA et al (2017) Design and application of 'J-shaped' stress-strain behavior in stretchable electronics: a review. Lab Chip 17(10):1689–1704. https://doi.org/10.1039/c7lc00289k
19. Ma Q, Cheng H, Jang KI et al (2016) A nonlinear mechanics model of bio-inspired hierarchical lattice materials consisting of horseshoe microstructures. J Mech Phys Solids 90:179–202. https://doi.org/10.1016/j.jmps.2016.02.012
20. Yan ZG, Wang BL, Wang KF et al (2019) A novel cellular substrate for flexible electronics with negative Poisson ratios under large stretching. Int J Mech Sci 151:314–321. https://doi.org/10.1016/j.ijmecsci.2018.11.026
21. Zhalmuratova D, La TG, Yu KTT et al (2019) Mimicking "J-Shaped" and anisotropic stress-strain behavior of human and porcine aorta by fabric-reinforced elastomer composites. ACS Appl Mater Interf 11(36):33323–33335. https://doi.org/10.1021/acsami.9b10524
22. Ray TR, Choi J, Bandodkar AJ et al (2019) Bio-integrated wearable systems: a comprehensive review. Chem Rev 119(8):5461–5533. https://doi.org/10.1021/acs.chemrev.8b00573
23. Ma YJ, Zhang YC, Cai SS et al (2020) Flexible hybrid electronics for digital healthcare. Adv Mater 32(15):23. https://doi.org/10.1002/adma.201902062
24. Lei M, Hong W, Zhao Z et al (2019) 3D printing of auxetic metamaterials with digitally reprogrammable shape. ACS Appl Mater Interf 11(25):22768–22776. https://doi.org/10.1021/acsami.9b06081
25. Xin X, Liu L, Liu Y et al (2020) 4D printing auxetic metamaterials with tunable, programmable, and reconfigurable mechanical properties. Adv Funct Mater 30(43):2004226. https://doi.org/10.1002/adfm.202004226
26. Wu WW, Hu WX, Qian GA et al (2019) Mechanical design and multifunctional applications of chiral mechanical metamaterials: a review. Mater Des 180:13. https://doi.org/10.1016/j.matdes.2019.107950
27. Wang ZW, Luan CC, Liao GX et al (2020) Progress in auxetic mechanical metamaterials: structures, characteristics, manufacturing methods, and applications. Adv Eng Mater 22(10):23. https://doi.org/10.1002/adem.202000312
28. Yu HB, Wu WW, Zhang JX et al (2019) Drastic tailorable thermal expansion chiral planar and cylindrical shell structures explored with finite element simulation. Compos Struct 210:327–338. https://doi.org/10.1016/j.compstruct.2018.11.043
29. Ruan X, Yuan W, Hu Y et al (2020) Chiral constrained stent: effect of structural design on the mechanical and intravascular stent deployment performances. Mech Mater 148:103509. https://doi.org/10.1016/j.mechmat.2020.103509
30. Farrugia PS, Gatt R, Grima-Cornish JN et al (2020) Tuning the mechanical properties of the anti-tetrachiral system using nonuniform ligament thickness. Phys Status Solidi B-Basic Solid State Phys 257(10):1900507. https://doi.org/10.1002/pssb.201900507
31. Liu J, Yao X, Wang Z et al (2021) A flexible porous chiral auxetic tracheal stent with ciliated epithelium. Acta Biomater 124:153–165. https://doi.org/10.1016/j.actbio.2021.01.044
32. Geng LC, Ruan XL, Wu WW et al (2019) Mechanical properties of selective laser sintering (SLS) additive manufactured chiral auxetic cylindrical stent. Exp Mech 59(6):913–925. https://doi.org/10.1007/s11340-019-00489-0
33. Liu J, Yan D, Zhang Y (2021) Mechanics of unusual soft network materials with rotatable structural nodes. J Mech Phys Solids 146:104210. https://doi.org/10.1016/j.jmps.2020.104210
34. Tufekci E, Ozdemirci O (2006) Exact solution of free in-plane vibration of a stepped circular arch. J Sound Vib 295(3–5):725–738. https://doi.org/10.1016/j.jsv.2006.01.048
35. Fan Z, Zhang Y, Ma Q et al (2016) A finite deformation model of planar serpentine interconnects for stretchable electronics. Int J Solids Struct 91:46–54. https://doi.org/10.1016/j.ijsolstr.2016.04.030
36. Babu AR, Gundiah N (2014) Role of crosslinking and entanglements in the mechanics of silicone networks. Exp Mech 54(7):1177–1187. https://doi.org/10.1007/s11340-014-9895-x
37. Nooni AR, Aslan TA, Temel B (2018) An efficient approach for in-plane free and forced vibrations of axially functionally graded parabolic arches with nonuniform cross section. Compos Struct 200:701–710. https://doi.org/10.1016/j.compstruct.2018.05.077
38. Greaves GN, Greer AL, Lakes RS et al (2011) Poisson's ratio and modern materials. Nat Mater 10(11):823–837. https://doi.org/10.1038/nmat3134
39. Wang D, Xiong Y, Zhang B et al (2020) Design framework for mechanically tunable soft biomaterial composites enhanced by modified horseshoe lattice structures. Soft Matter 16(6):1473–1484. https://doi.org/10.1039/c9sm02119a
40. Hoffman B, Martin M, Brown BN et al (2016) Biomechanical and biochemical characterization of porcine tracheal cartilage. Laryngoscope 126(10):E325–E331. https://doi.org/10.1002/lary.25861
41. Xue ZG, Song HL, Rogers JA et al (2020) Mechanically-guided structural designs in stretchable inorganic electronics. Adv Mater 32(15):32. https://doi.org/10.1002/adma.201902254

42. Zhu YZ, Joralmon D, Shan WT et al (2021) 3D printing biomimetic materials and structures for biomedical applications. Bio-Des Manuf 4(2):405–428. https://doi.org/10.1007/s42242-020-00117-0
43. Safshekan F, Tafazzoli-Shadpour M, Abdouss M et al (2020) Finite element simulation of human trachea: normal vs. surgically treated and scaffold implanted cases. Int J Solids Struct 190:35–46. https://doi.org/10.1016/j.ijsolstr.2019.10.021
44. Wang YE, Guo Y, Wei QH et al (2021) Current researches on design and manufacture of biopolymer-based osteochondral biomimetic scaffolds. Bio-Des Manuf 4(3):541–567. https://doi.org/10.1007/s42242-020-00119-y
45. Ahn CB, Son KH, Yu YS et al (2019) Development of a flexible 3D printed scaffold with a cell-adhesive surface for artificial trachea. Biomed Mater 14(5):9. https://doi.org/10.1088/1748-605X/ab2a6c
46. She YL, Fan ZW, Wang L et al (2021) 3D printed biomimetic pcl scaffold as framework interspersed with collagen for long segment tracheal replacement. Front Cell Dev Biol 9:14. https://doi.org/10.3389/fcell.2021.629796
47. Askari M, Hutchins DA, Thomas PJ et al (2020) Additive manufacturing of metamaterials: A review. Addit Manuf 36:101562. https://doi.org/10.1016/j.addma.2020.101562
48. Lin M, Firoozi N, Tsai CT et al (2019) 3D-printed flexible polymer stents for potential applications in inoperable esophageal malignancies. Acta Biomater 83:119–129. https://doi.org/10.1016/j.actbio.2018.10.035
49. Hamzehei R, Rezaei S, Kadkhodapour J et al (2020) 2D triangular anti-trichiral structures and auxetic stents with symmetric shrinkage behavior and high energy absorption. Mech Mater 142:10. https://doi.org/10.1016/j.mechmat.2019.103291

Authors and Affiliations

Jiapeng Liu[1,2] · Xinhua Yao[1,2] · Zhenwei Wang[1,2] · Jian Ye[3] · Congcong Luan[1,2] · Jianzhong Fu[1,2] · Yong He[1,2]

✉ Xinhua Yao
yaoxinhuazju@gmail.com

✉ Jian Ye
yejianchi@126.com

[1] State Key Laboratory of Fluid Power and Mechatronic Systems, College of Mechanical Engineering, Zhejiang University, Hangzhou 310027, China

[2] Key Laboratory of 3D Printing Process and Equipment of Zhejiang Province, College of Mechanical Engineering, Zhejiang University, Hangzhou 310027, China

[3] Department of Pneumology, Affiliated Hangzhou First People's Hospital, Zhejiang University School of Medicine, Hangzhou 310006, China